Assessing the shielding of engine noise by the wings for current aircraft using model predictions and measurements

Alves Vieira, A.E.; Snellen, Mirjam; Simons, Dick G.

DOI
10.1121/1.5020798

Publication date
2018

Document Version
Accepted author manuscript

Published in
Journal of the Acoustical Society of America

Citation (APA)
Alves Vieira, A. E., Snellen, M., & Simons, D. G. (2018). Assessing the shielding of engine noise by the wings for current aircraft using model predictions and measurements. *Journal of the Acoustical Society of America*, *143*(1), 388-398. https://doi.org/10.1121/1.5020798

Assessing the shielding of engine noise by the wings for current aircraft using model predictions and measurements

Ana Vieira,[1] Mirjam Snellen,[1] and Dick G. Simons[1]
Section Aircraft Noise and Climate Effects, Faculty of Aerospace Engineering, Delft University of Technology, 2629 HS Delft, The Netherlands

Reducing aircraft noise is a major issue to be dealt with by the aerospace industry. In addition to lowering noise emissions from the engine and airframe, also the shielding of engine noise by the aircraft is considered as a promising means for reducing the perceived noise on the ground. In literature, noise shielding predictions indicate significant reductions in received noise levels for Blended Wing Body configurations, but also for conventional aircraft with the engines placed above the wings. Little work has been done in assessing these potential shielding effects for full aircraft under real operational conditions. Therefore, in this work, noise shielding for current aircraft is investigated using both measurements and model predictions. The predictions are based on the Kirchhoff integral theory and the Modified Theory of Physical Optics (MTPO). Twenty Fokker 70 flyovers are considered for the comparison between the predictions and measurements. The data analysis approach for the extraction of shielding levels for aircraft under these operational conditions is presented. Directly under the flight path, the simulations predict an engine noise shielding of 6 dB overall sound pressure level. This is confirmed by some of the flyover data. On average, the measurements show somewhat lower shielding levels.

 [http://dx.doi.org(DOI number)]

[XYZ] Pages: 1–12

List of Symbols

λ	=	wavelength
ξ	=	detour parameter (singularity of the potential I_Γ)
$\boldsymbol{\rho}$	=	vector from source position to diffraction edge
σ	=	aperture in the screen
$\overline{\sigma}$	=	screen
χ	=	equal to 1 if the ray goes through the aperture and 0 otherwise
Att_i	=	attenuation per frequency
Att_{ave}	=	total attenuation averaged over frequency
$\mathbf{e}$	=	unit direction of line segment
f	=	frequency
f(s)	=	amplitude function
F	=	Fresnel integral
g(s)	=	phase function
I_Γ	=	diffraction potential
k	=	wave number
N_{freq}	=	number of frequencies considered in the spectrum
$p^{Aperture}$	=	scattered pressure field in an aperture in a screen
p_d	=	diffracted pressure field
p_i	=	incident pressure field
$p^{Obstacle}$	=	scattered pressure field around a shielding object
p_s	=	scattered pressure field
$\mathbf{r}$	=	vector from observer position to diffracting edge
$\mathbf{R}$	=	vector between source and receiver position
$\mathbf{s_a}$	=	start point of a segment
$\mathbf{s_b}$	=	end point of a segment
t	=	detour paramter for the Fresnel integral
$\mathbf{x}$	=	receiver position
$\mathbf{x^Q}$	=	source position
$\mathbf{y}$	=	point in the screen
$\mathbf{y_0}$	=	arbitrary initial point in a segment
OSPL	=	Overall Sound Pressure Level
SPL	=	Sound Pressure Level

I. INTRODUCTION

Air traffic has been continuously expanding over the last decades and statistics indicate that the number of passengers is expected to double by 2050. Noise nuisance resulting from air traffic is known to affect human health[1,2] and for that reason airports are subjected to strict regulations that limit their capacity and operative hours. The expected growth of air traffic will aggravate this situation so that aircraft noise reduction is an important research field.

Despite all the improvements in turbofan engines since the 1960's[3], engines are still a major source of noise. Consequently, one possible strategy to further reduce the perceived engine noise on the ground is through acoustic

shielding, which occurs when there is a barrier between the source and observer.

Predictions of noise reductions due to the shielding of engine noise were found promising for Blended Wing Body (BWB) configurations, but also for wing and tube aircraft[4–6]. In these references, high values of noise attenuation were reported. The predictions were compared with wind-tunnel data using model aircraft[5,7] or with other computational tools[4]. These comparisons show good agreement and as such the predictions further strengthen the potential of using shielding as a way to contribute to lowering aircraft noise levels at the ground.

In this paper we investigate the influence of noise shielding in conventional tube and wing aircraft with overwing engines, so that the engine noise can be shielded by the wings. The focus is on aircraft that are currently in operation and both predictions and measurements are used to assess noise shielding. For the predictions a method is used which is based on the Kirchhoff integral theory[8] and the Modified Theory of Physical Optics (MTPO)[9,10].

This MTPO based method was found to give a good trade-off between accuracy and computational time in the specific case of full-scale aircraft[9]. Other methods, such as the Boundary Element Method (BEM)[11], the Equivalent Source Method[12] and the Ray-tracing method[13], are considered to be more accurate and can be used for smooth objects but are computationally demanding. On the other hand, a widely used semi-empirical method, called the Barrier Shielding Method (BSM)[8,14] is fast, but does not provide the flexibility and accuracy desired.

For the measurements use is made of data measured from real aircraft flyovers, i.e. full-scale aircraft under operational conditions. The Fokker 70 was selected for the comparison of the model predictions with the flyover measurements since for this aircraft the engines are above the wings and close to their surface, and therefore significant noise shielding is expected. We introduce an innovative data analysis approach to extract the noise shielding levels for these flyovers. In addition, the engine noise spectrum used in the predictions is derived from the measurements. This contributes to more realistic results than what is currently often found in literature, where, in the absence of the engine spectrum, the values of noise attenuation due to shielding are averaged over frequency assuming equal noise levels for all frequencies.

Section II presents the theory of the MTPO based method, used to calculate noise shielding. The results are compared with predictions from other methods for canonical cases. Section III compares experimental data of flyovers of several aircraft types and assesses if there is evidence of noise shielding in aircraft with the engines mounted above the wings. Section IV shows the results of the noise shielding predictions for the Fokker 70. In addition, we present shielding predictions for the McDonnell Douglas 81, showing the effect of a different engine/wing configuration. Section V compares the predictions for the F70 with flyover measurements and Section VI presents a summary of the paper and the main conclusions.

II. NOISE SHIELDING PREDICTION METHOD

A. Theory

Noise shielding for aircraft occurs mainly due to diffraction of engine noise by the wings. When assessing this shielding through modelling, the wing surface is usually approximated as a flat plate because of the large chord and span dimensions relative to its thickness.

A common approach for calculating noise shielding is the Barrier Shielding Method (BSM)[14–16]. This semi-empirical method is based on experimental measurements of Maekawa[14] of a thin half-infinite barrier and can be applied to a wing geometry taking into consideration three instead of a single diffraction edge. This approach was implemented, for example, in the ANOPP model from NASA[17].

The BSM is not computationally expensive or complex to implement and, therefore, it is a popular method for calculating noise shielding on sharp-edged objects. This method provides a fast approximation of noise attenuation but has several limitations. Firstly, the method is empirical and not based on first principles, and it is only valid for monopole sources. In addition, the BSM method has a limited range of applications because it is only applicable to geometries that can be approximated by semi-infinite screens.

An alternative to the BSM that is not as complex and computationally expensive as the Boundary Element Method (BEM)[18] and the Equivalent Source Method (ESM)[12] (considered the most accurate methods) is the Ray-tracing method. However, also for the Ray-tracing method the computational cost for calculating creeping rays is rather high. Another alternative is a method based on the Kirchhoff integral theory and built on the Modified Theory of Physical Optics (MTPO)[9,10].

Consider an arbitrary aperture σ in a screen $\overline{\sigma}$ located between a source placed at $\mathbf{x}^{\mathbf{Q}}$ and a receiver position $\mathbf{x}$, as represented in Fig.1.

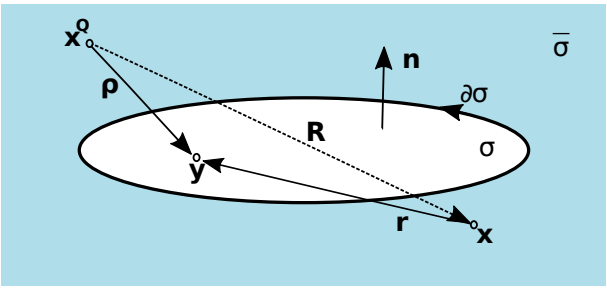

FIG. 1. Kirchhoff integration across the circular aperture σ in the screen $\overline{\sigma}$.

Both the scattered field p_s, and the field emitted by the source p_i follow the Helmholtz equation in a volume of control that does not include the screen surface and the source location. The system of equations can be rewritten applying the Gauss and Green theorems on the referred volume of control and further simplified using approximations in the boundary conditions. The scattered field p_s is considered zero on the screen, meaning that the shielding object is at rest and in a non-oscillatory state. Also, the scattered field approximates zero for large enough range from the source and equals to p_i in the aperture.

The pressure field at the receiver position $\mathbf{x}$ can then be obtained by the calculation of the Kirchhoff integral over the aperture σ,

$$p_s^{Aperture} = \frac{1}{4\pi}\int_\sigma \left[p_i \mathbf{n}\cdot\nabla\frac{e^{ik|\mathbf{r}|}}{|\mathbf{r}|} - \frac{e^{ik|\mathbf{r}|}}{|\mathbf{r}|}\mathbf{n}\cdot\nabla p_i\right] dS, \tag{1}$$

where $\mathbf{r} = \mathbf{y} - \mathbf{x}$, $\mathbf{y}$ is located at the aperture and k is the wavenumber.

The evaluation of the surface integral of Eq.1 is computationally expensive, so the theory of boundary diffracted waves is introduced to simplify it[8]. The theory of boundary diffracted waves states that the scattered field is given by the undisturbed incident field p_{GO} and the boundary diffracted field p_d. This can be written as

$$p_s^{Aperture} = p_{GO} + p_d. \tag{2}$$

Here $p_{GO} = p_i\chi$, where χ is a delta function equal to unity when the ray from source to receiver passes through the aperture σ and zero otherwise.

The boundary diffracted wave theory depends only on the outline of the shielding object $\partial\sigma$, so it can be expressed as a line integral as it will be shown next.

Maggi and Rubinowicz[19] considered a monopole source and a control volume that is defined by rays originating from the source that touch the aperture $\partial\sigma$, as represented in Fig.2.

Based on this approach, they derive the following expression for the diffracted field p_d, written in terms of a line integral along $\partial\sigma$,

$$p_d = \frac{1}{4\pi}\oint_{\partial\sigma}\frac{e^{ik|\boldsymbol{\rho}|}}{|\boldsymbol{\rho}|}\frac{e^{ik|\mathbf{r}|}}{|\mathbf{r}|}\frac{(\boldsymbol{\rho}\times\mathbf{r})\cdot d\mathbf{s}}{|\boldsymbol{\rho}||\mathbf{r}| + \boldsymbol{\rho}\cdot\mathbf{r}}, \tag{3}$$

where $\boldsymbol{\rho} = \mathbf{x} - \mathbf{x^Q}$.

The integration contour can be discretized in straight line segments, described by,

$$\mathbf{y}(s) = \mathbf{y_0} + s\mathbf{e}, \qquad s_a < s < s_b, \tag{4}$$

where $\mathbf{y_0}$ is an arbitrary initial point, $\mathbf{e}$ is the unit direction of the segment and s_a and s_b are the start and end points of the segment.

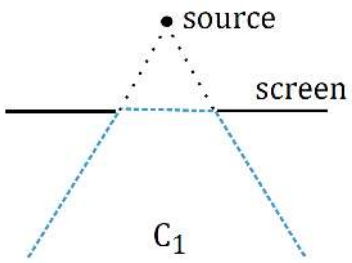

FIG. 2. Volume of control,C_1, used in the Maggi Rubinowicz formulation, indicated by the dashed lines.

Considering a straight line segment Γ, described by Eq.4, the diffraction line integral can be re-written as a Fourier integral as

$$I_\Gamma = \frac{1}{4\pi}\int_\Gamma \frac{1}{|\boldsymbol{\rho}|}\frac{1}{|\mathbf{r}|}\frac{(\boldsymbol{\rho}\times\mathbf{r})\cdot d\mathbf{s}}{|\boldsymbol{\rho}||\mathbf{r}| + \boldsymbol{\rho}\cdot\mathbf{r}} e^{ik(|\mathbf{r}|+|\boldsymbol{\rho}|)} = \int_\Gamma f(s)e^{ikg(s)ds}, \tag{5}$$

where $f(s)$ and $g(s)$ are, respectively, the amplitude and phase of the function to be integrated.

The integral will be evaluated using the method of the stationary phase (see Appendix A1), which introduces a singularity in the contribution of the endpoints. To deal with this singularity, the Uniform Theory of Diffraction[20] is introduced. The Uniform Theory of Diffraction states that the scattered field behaves like a Fresnel integral in the transition points between segments along the contour of the aperture. This theory is motivated by the exact solution derived by Sommerfeld to the canonical problem of a plane wave diffraction by a semi-infinite plate[21]. A so-called 'detour' parameter is introduced as a change of variable as well as the fundamental property of the Fresnel integral to describe the diffracted field (Appendix A2). The line integral of the segment Γ can then be written as,

$$\begin{aligned} I_\Gamma = \sqrt{\pi}e^{i\frac{\pi}{4}}e^{ikg(s^*)}\{&G(s^*)(U(-t(s_a)) - U(-t(s_b)) \\ &+ G(s_a)sign(t(s_a))F[|t(s_a)|] - G(s_b)sign(t(s_b))F[|t(s_b)|]\} \end{aligned} \tag{6}$$

Here s^* is the stationary phase point, U is the unit step function, t is the detour parameter, $G(s) = f(s)/h(s)$ and the Fresnel integral is given by

$$F[x] = \frac{e^{-i\frac{\pi}{4}}}{\sqrt{\pi}}\int_x^\infty e^{it^2}dt, \tag{7}$$

and its asymptotic expansion is

$$sign(x)F[|x|] \simeq \frac{e^{i\frac{\pi}{4}}}{2\sqrt{\pi}}\frac{e^{ix^2}}{x}. \tag{8}$$

At this point the integral I_Γ still contains the singularity when $|\boldsymbol{\rho}||\mathbf{r}| + \boldsymbol{\rho}\cdot\mathbf{r} = 0$. Using another detour parameter, ξ, it is possible to identify the asymptotic expansion of the Fresnel integral in Eq.6 and replace it by the actual function (see Appendix A3), which results in the following expression,

$$I_\Gamma = 2\sqrt{\pi}\xi sign(\xi)F[|\xi|]\{G(s^*)[U(-\xi_a) - U(-\xi_b] + G(s_a)sign(\xi_a)F[|\xi_a|] - G(s_b)sign(\xi_b)F[|\xi_b|]\}. \quad (9)$$

Here the detour parameter $\xi(s,P) = \epsilon_\xi(P)\sqrt{k[g(s) - |\mathbf{R}|]}$ and ϵ_ξ is a shadow indicator equal to 1 if point P is located in the illuminated region and -1 if in the shadow.

The diffraction field through an arbitrary aperture can now be evaluated by discretizing the edge of the aperture into linear edges and by adding the results of Eq.10 for each edge.

At this point the $p_s^{Aperture}$ can be calculated since p_i is known a priori and p_d is calculated using the procedure described above. In order to obtain the scattered field due to the presence of an object, p_s^{object}, one can make use of Babinet's principle, and interchange the obstacle with the aperture in the screen,

$$p_s^{Object} = p_i - p_s^{Aperture}. \quad (10)$$

A common way of presenting the noise reduction due to shielding is based on the so-called shielding factor ΔSPL, given by

$$\Delta SPL = -20log_{10}\left|\frac{p_s^{Object}}{p_i}\right|. \quad (11)$$

B. Comparison with other noise shielding calculation methods

A first validation of the noise shielding predictions was obtained by comparing its results with cases available in literature from other noise shielding predictions.

Let us consider the case of a circular disk as represented in Fig.3, with $a = 1$ and $k = 92$ m^{-1} ($f = 5000$ Hz). Fig.4a) illustrates the result obtained by NASA's Fast Scattering Code[7] and by the implementation of the MTPO method of Ng et al[9]. Fig.4b) shows the results obtained with the implementation of the MTPO-based method used in this work.

The red mark in the plot on the right indicates the x-coordinate that separates the shadow-light contour of the disk on the observer plane. From this point forward the observers are not affected by noise shielding, and attenuation will oscillate around 0 dB.

Let us consider now a strip with a length of 10 m and width of 2 m. A monopole source is centered above the strip, and the source and observers position are at the same relative distances as in the case of the disk. The results of noise shielding obtained with the BEM and the Ray-Tracing method (for $\lambda = 0.2$ m) are represented in Fig.5a) and are taken from the work of Lummer et al[4].

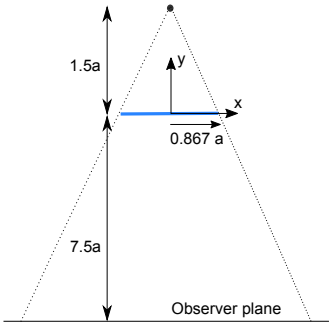

FIG. 3. Disk configuration for the validation of the MTPO-based method.

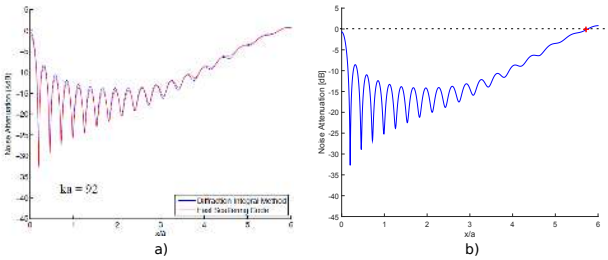

FIG. 4. Disk shielding for $ka = 92$: a) from Ng et al[9] and b) calculated in this work using the MTPO-based method.

Fig.5b) shows the results obtained with the MTPO based method using the code developed in this work.

Both Fig.4 and Fig.5b) show the good agreement between the MTPO based method and results from other noise shielding tools for different flat geometries. As expected, the MTPO based method gives closer results to the Ray-tracing method, since they are both high frequency approximations.

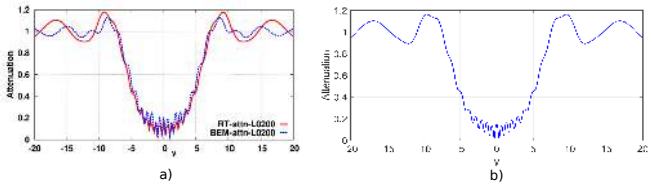

FIG. 5. Stripe shielding for λ=0.2 m: a) obtained with the BEM and the Ray-tracing method[4], b) calculated in this work using the MTPO-based method.

III. ASSESSING NOISE SHIELDING FROM MEASUREMENTS OF AIRCRAFT FLYOVERS

Previous research identified a promising reduction of aircraft noise levels due to the shielding of the engine noise by the aircraft fuselage and wings[6,17]. In this contribution we aim to further assess these noise shielding predictions with real aircraft flight data.

The experimental data used consists of a set of flyovers of different aircraft types recorded using a 32 microphone array arranged in a spiral distribution[22,23]. The diameter of the array is 1.7 m. The data is band filtered in the frequency range 45 Hz - 11,200 Hz and was acquired with a sample frequency of 40 kHz. The measurements were taken at Amsterdam Airport Schiphol during two days with similar weather conditions and low wind speed. To assess the aircraft speed and height, an optical camera was placed at the centre of the array facing straight up from the ground. The array was located 1,240 m to the South of the threshold of the Aalsmeerbaan runway (36R), mainly used for landing. The position was selected to be directly underneath the path of the landing aircraft, so that the aircraft flew directly over the array.

The aircraft for which flyovers were recorded are listed in Table I. The altitude and the flight velocity are determined from measurements taken by the optical camara, radar data and Automatic Dependent Survaillance-BroadCast (ADS-B) data[24]. The flight velocities were around 75 m/s and the height above the array was about 67 m. From this list, noise shielding is expected to occur for the Fokker 70 and McDonnell Douglas 81 because their engines are mounted above the wings, as indicated in the second column of Table I.

The aircraft height, speed and engine settings are assumed to remain stationary during each flyover. For all flyovers the Overall Sound Pressure Level (OSPL) was determined as a function of time for each of the 32 microphones in the array and then averaged over the microphones. The OSPL values will differ for each aircraft due to the variation of aircraft types considered. Typically the larger aircraft (A380, B747) show significantly higher levels. To still be able to compare the variation of OSPL as a function of time for the different aircraft, a normalization step is applied where for each aircraft the maximum OSPL as measured for that aircraft is subtracted from the OSPL levels. This normalization of the OSPL versus time curve renders the shape of the curve. Fig.6 shows the resulting normalized OSPL versus time, where the value zero corresponds to the maximum value of OSPL for each flyover.

In the work of Simons et al[25] the results of a noise breakdown for the flyovers of Table I are presented, based on 1) beamforming of the data through which the individual noise sources on the aircraft are revealed, 2) the data spectograms, and 3) a model-data comparison for each of the aircraft. From this noise breakdown it was concluded that for these flyovers, the received sound levels are dominated by engine noise. As a result of this finding we postulate that the OSPL values as shown in Fig.6 reflect the aircraft engine noise.

Based on this insight, two important conclusions can be drawn from Fig.6. Firstly, it is seen that all curves for the aircraft without shielding almost coincide, despite the fact that they all have different engines. This indicates that these aircraft show similar variations of OSPL versus time, and thus polar angle. Consequently, it is concluded that differences in the polar directivity of the engine noise for various aircraft types can be neglected when comparing the normalised OSPL curves. The x-axis is normalised relatively to the overhead time and the y-axis is normalised by the maximum value of OSPL.

Secondly, the two aircraft types for which shielding is expected are below all other curves, especially in the phase where intuitively shielding is expected as the aircraft is approaching the array.

Based on the above two observations it is postulated that the differences in the curves of Fig.6 are due to shielding of the engine noise by the wings and fuselage.

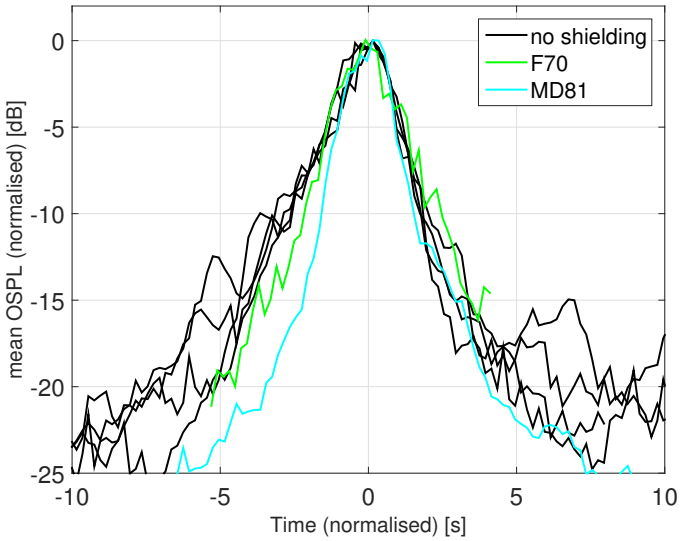

FIG. 6. Measured OSPL (normalised and averaged over the 32 microphone array) as a function of time for flyovers (landing) of a variety of aircraft types.

IV. NOISE SHIELDING PREDICTIONS

As a next step to assess the effects of shielding, model predictions are carried out. The engine locations for the F70 and the MD81 were determined using beamforming methods[22,24,26], which resulted in the plots of Fig.7. The location of the engines and the aircraft contours used for the predictions, based on the beamforming plots, are shown in Fig.8.

Based on the assumptions introduced above regarding the dominance of engine noise, the measured spectrum is assumed to fully represent the noise emitted by

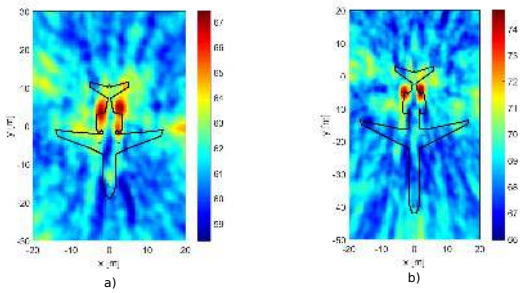

FIG. 7. Beamforming plots for high frequency band: (a) F70 (b) MD81[25].

FIG. 8. Limit shadow-light and source position used in the predictions for (a) the F70 (b) the MD81.

the engine. The dominance of the engine noise is particularly evident for high frequencies, in the region of the hump of Fig.9 (for these aircraft the contribution of airframe noise is significant in lower frequencies[25]).

For the model predictions the spectrum is approximated for the 1/3-octave bands, as illustrated in Fig.9 by the dashed line, for the case of the F70 engines.

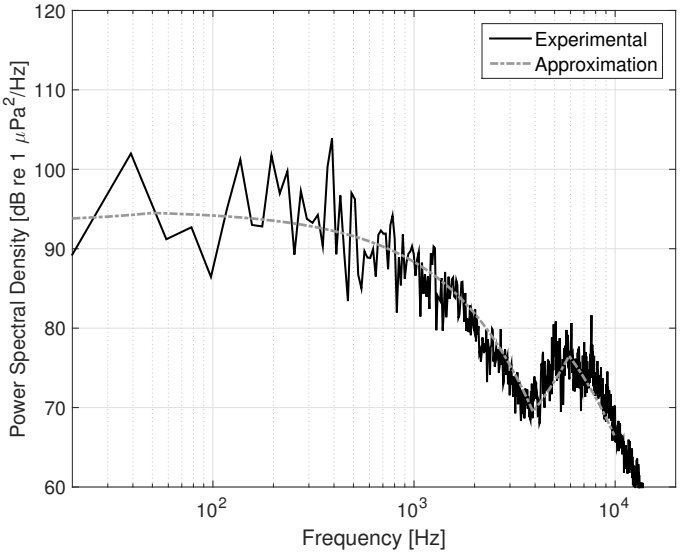

FIG. 9. Frequency spectrum of the F70 engines. The black line indicates the measured spectrum and the gray line its approximation.

The attenuation in Eq.11 is calculated per frequency. In general, the total attenuation is presented as an average of the values found for the central 1/3-octave bands frequencies as

$$Att_{ave} = \frac{1}{N_{freq}} \sum_{i=1}^{N_{freq}} Att_i, \tag{12}$$

where Att_{ave} is the average attenuation for all frequencies considered, N_{freq}, and Att_i is the attenuation value found per frequency.

This way of presenting noise attenuation is practical because the source strength is not necessary. However, as expected, some frequencies are more attenuated (high frequency range) and that fact is not reflected by Eq.12. In this work, as referred before, the source spectrum is known, so there is no need of using Eq.12. Nevertheless, for completeness, also Eq.12 is used to quantify the noise shielding.

Consider Figs.10 and 11, representing the OSPL at a grid of observers on the ground for the F70 and the MD81 (the aircraft orientation is from the right to the left of the plot). The plots of Fig.10 were calculated using Eq.12 and in Fig.11 the ΔSPL was applied per frequency. The two methods of calculating the OSPL with noise shielding show major differences, and the values of the OSPL are much lower in Fig.10 than in Fig.11.

This indicates that Eq.12, commonly used in literature, results in higher values of noise attenuation that might not be realistic as it is dominated by frequencies that are not dominant in the emitted noise. This will be further investigated by comparing the computational results with experimental data.

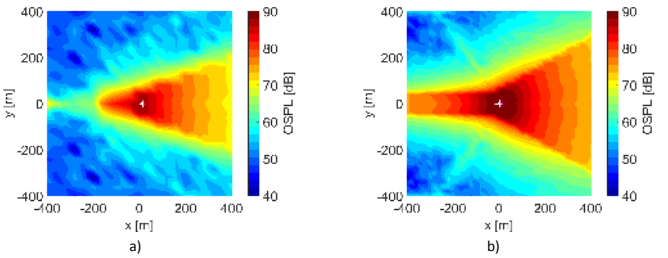

FIG. 10. OSPL calculated with averaged attenuation values, in a grid of observers on ground a) for the F70, b) for the MD81.

Fig.12a) and 12b) show the change in OSPL at the receiver positions when considering the values of Fig.11a) and Fig.11b), respectively, relative to the OSPL calculated without taking noise shielding into consideration.

In Fig.12a) the largest reductions in $OSPL$ are found for receivers ahead of the aircraft. The projection of the shape of the wings is clearly visible in the plot. However, outside that area also significant shielding effects

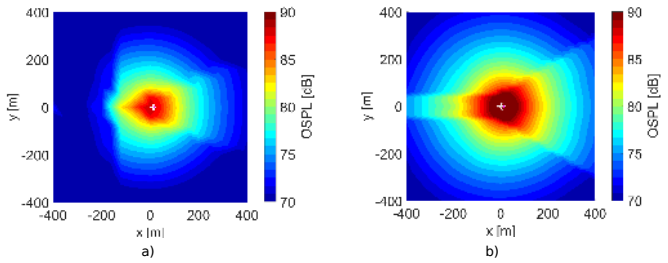

FIG. 11. OSPL calculated subtracting attenuation at each frequency in a grid of observers on ground, a) for the F70 b) for the MD81.

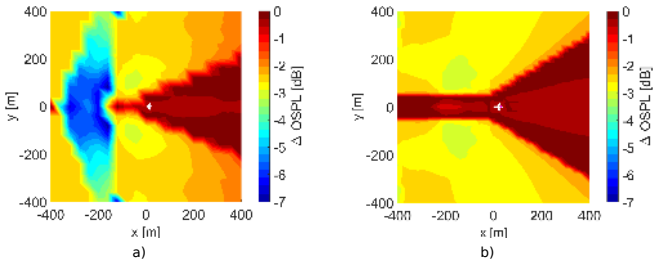

FIG. 12. ΔOSPL in a grid of observers on ground, a) for Fig.11a) (F70), b) for Fig.11b) (MD81) .

are found, despite being lower, around -3/-2dB. This plot indicates that for the case of the F70 noise shielding plays an important role and neglecting it will cause discrepancies between predictions and experimental measurements of noise levels.

For the F70 the engines are located closer to the wings than for the MD81 and therefore lower values of noise shielding are expected for the MD81. The plots of Fig.12a) and Fig.12b) support that assumption, with maximum values of noise shielding around -4 dB for the MD81 and -7 dB for the F70.

The shape of the plot is also very distinct when compared with the one of the F70, and the projection of the wings in the plot is not as clear. In the MD81 the values of attenuation are higher to the sides of the aircraft than that to the front. This distinct behaviour is the consequence of a different engine location, more on the back of the rear fuselage.

However, the OSPL curve of the MD81 of Fig.6 seems to indicate higher values of noise shielding in this aircraft than the F70, and for a longer period of time. It is worth to mention that the MD81 has low-bypass-ratio engines with target-type thrust reversers. This differs from the high-bypass-ratio engines with cascade thrust reversers that all the other aircraft presented in Fig.6 are equipped with. It is hypothesized that this results in a different shape of the engine directivity of the MD81[27], and thus this strong directivity, unlike the other aircraft considered in this work, cannot be neglected in the OSPL curve. This hypothesis cannot be further investigated as only a single flyover is available for the MD81.

V. MODEL-DATA COMPARISON

In this section the predictions will be compared with experimental data. The comparison will be focused on the F70, because in the experimental campaign referred to in Section III, 20 flyovers of the F70 were recorded and only a single MD81 flyover.

For the comparison of the predicted noise shielding of Fig.12a) with the experimental data, the OSPL as a function of time is considered. Figs.13 to 16 show the measured OSPL of 4 flyovers (from a total of 20 flyovers analysed in this work) together with the predictions (with and without noise shielding). Notice that for the prediction with shielding the OSPL is calculated by subtracting the attenuation per frequency. These 4 flyovers were selected because they are representative of all the flyovers analysed.

Fig.13 and 14 represent two of the flyovers with relatively good agreement with the predictions. One can observe that when comparing the predictions with and without shielding there is a distinct period in time (i.e. angle of the aircraft with respect to the observer) where the values for these two cases differ. It is only at these moments that the engine noise is shielded. This region is in very good agreement with the measurements. Also the predicted decrease in noise levels agrees well with that observed experimentally, although slighlty overpredicted.

Fig.15 illustrates an intermediate example, in which the measurements show less noise shielding than predicted. Finally, Fig.16 represents one flyover with no evidence of noise shielding in the measurements.

Fig.17 summarizes the measured values of OSPL for all flyovers analysed, as well as the predicted value of shielding and the average of the values of shielding found experimentally. The value zero on the plot means that no noise shielding was found present for the flyover.

There is clear evidence of noise shielding in many of the flyovers analysed. However, a very substantial amount of the measurements does not show shielding. In the flyovers in which noise shielding was found the time period in which it occurs agrees with the predictions in all the cases. This is a strong evidence that the distinct OSPL curve behaviour of the F70 is due to noise shielding as postulated in Section III.

It is assumed that the variability of the results can be attributed to simplifications of the flight trajectory and engine settings here considered. In addition, some of the measurements contained significant background noise, see e.g. Fig.16.

It can then be concluded that noise shielding is relevant in the case of the F70, as expected considering the predictions, and now supported by the experimental data. The observer position is aligned with the landing flyover and centered at the aircraft fuselage and in that position, as can be observed in Fig.13 to 16, noise

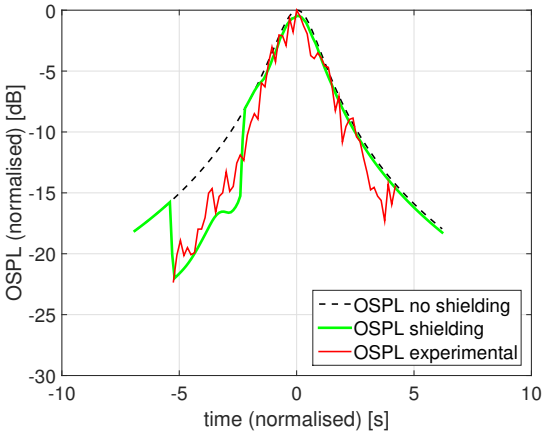

FIG. 13. Measured OSPL for Flyover 1 of the F70 and predictions with and without noise shielding.

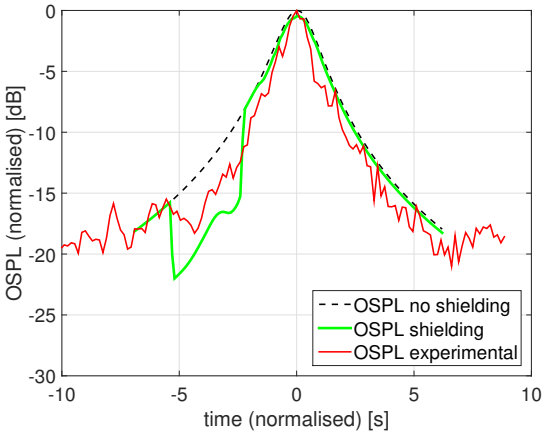

FIG. 14. Measured OSPL for Flyover 19 of the F70 and predictions with and without noise shielding.

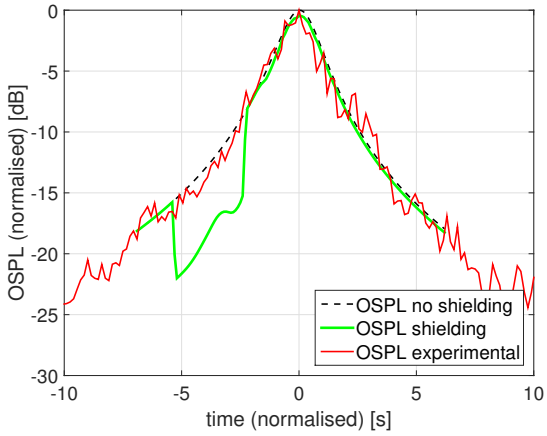

FIG. 15. Measured OSPL for Flyover 11 of the F70 and predictions with and without noise shielding.

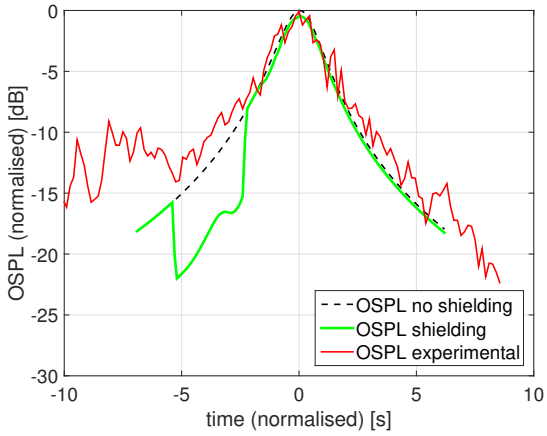

FIG. 16. Measured OSPL for Flyover 7 of the F70 and predictions with and without noise shielding.

shielding only occurs during a very limited period of time. However, the numerical results indicate that, for a receiver position not aligned with the aircraft trajectory, noise shielding occurs during longer periods of time, as can be observed in Fig.18. Therefore, noise shielding should be accounted for when calculating noise contours on ground of aircraft with engines above the wings.

VI. SUMMARY AND CONCLUSIONS

In this research a computational tool was developed for predicting noise shielding of the engine by the aircraft airframe. A method based on the Kirchhoff integral theory and the MTPO was used for the predictions. This method was recently developed[9] and its implementation was validated based on canonical cases for sharp-edged geometries as is the case of the aircraft wings, which are the most important aircraft components for engine noise shielding.

Predictions of noise shielding were carried out for the F70 and the MD81, and it was shown, as expected, that the values of noise shielding are higher for the F70 because the engines are located closer to the wings than in the MD81.

The predictions of noise shielding were compared with experimental data for the F70 aircraft in terms of the OSPL curve during the flyover for a set of 20 measurements.

In the absence of the frequency spectrum of the source, the attenuation due to shielding is commonly predicted as the average over the 1/3 octave-bands. In this work, the source frequency spectrum, determined from flyover measurements, was used. Hence, for the predictions, it was possible to apply the attenuation per frequency and thus calculate the OSPL including shielding that can directly be compared with the measured OSPL.

The values of noise attenuation were found to be higher in the predictions than in the experimental data. For the F70 an average reduction of 6 dB was predicted in the perceived noise and experimentally the value was $2.7 \pm 1.7\ dB$, in the time interval in which there is noise shielding for an observer aligned with the flight trajec-

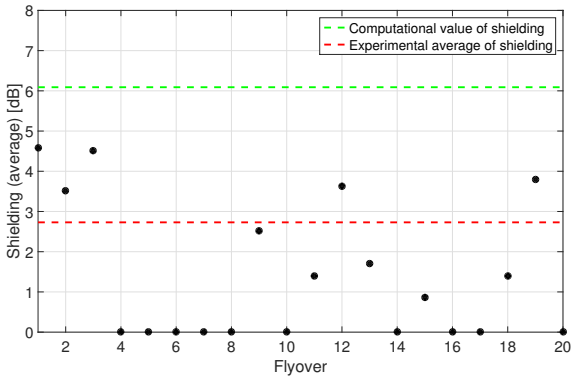

FIG. 17. Measured and predicted value of noise shielding found for different flyover measurements of the F70. The dots indicate the shielding for the 20 flovers and the red dashed line - - - indicates the average value of the flyovers with noise shielding. The green dashed line - - - is the predicted value of shielding.

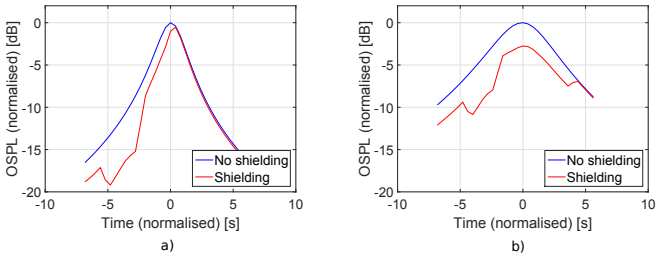

FIG. 18. Predictions of OSPL with and without taking noise shielding into consideration for an observer at a distance of a) 40 m and b) 160m, from the aircraft centerline (F70).

tory. This difference is at least partly resulting from the imperfect modelling of the aircraft geometry and the exact flight conditions. Also, for some flyover data the background noise is hampering the extraction of shielding levels from the data.

The values of noise shielding are significant and should be taken into consideration in the predictions of noise levels on ground. However, this work demonstrates that the noise attenuation averaged over the frequency, used in previous works, results in an overestimation of noise shielding. Therefore, the spectrum of the noise source needs to be used in order to obtain realistic values of noise shielding.

APPENDIX A:

1. Method of the Stationary Phase

Consider the notation introduced by Lummer[4] to express the discretization of the diffraction problem,

$$\mathbf{y_0} = \mathbf{y} - s\mathbf{e} \quad \mathbf{a} = \mathbf{y_0} - \mathbf{x^Q}, \quad \mathbf{b} = \mathbf{y_0} - \mathbf{x_u} = \mathbf{a} \times \mathbf{b}, \quad \mathbf{v} = \mathbf{e} \times (\mathbf{a} - \mathbf{b})$$

$$\mathbf{a}^2 = \mathbf{a} \cdot \mathbf{a}, \quad \mathbf{b}^2 = \mathbf{a} \cdot \mathbf{b}, \quad \alpha = \mathbf{a} \cdot \mathbf{e}, \quad \beta = \mathbf{b} \cdot \mathbf{e}, \gamma = \mathbf{a} \cdot \mathbf{b}$$

$$\boldsymbol{\omega} = \mathbf{a} \times \mathbf{e}, \quad \mathbf{z} = \mathbf{v} + \mathbf{w}$$

$$\boldsymbol{\rho} = \mathbf{a} + \mathbf{e}s, \quad \mathbf{r} = \mathbf{b} + \mathbf{e}s$$

$$\boldsymbol{\rho}^2 = \mathbf{a}^2 + 2\alpha s + s^2, \quad \mathbf{r}^2 = \mathbf{b}^2 + 2\beta s + s^2$$

$$\boldsymbol{\rho} \cdot \mathbf{r} = \gamma + (\alpha + \beta)s + s^2, \quad (\boldsymbol{\rho} \times \mathbf{r}) \cdot d\mathbf{s} = (\mathbf{a} \times \mathbf{b}) \cdot \mathbf{e} ds$$

The curvelinear abcissa of the stationary phase s^* is given by,

$$s^* = -\frac{|\boldsymbol{\omega}|\beta + |\mathbf{z}|\alpha}{|\boldsymbol{\omega}| + |\mathbf{z}|}. \tag{A1}$$

If the phase function $g(s)$ does not have any stationary phase points inside the segment Γ, the asymptotic expansion can be obtained by integration by parts as expressed in Eq.A2,

$$I_\Gamma = \frac{1}{ik}\left[\frac{f(s_b)}{g'(s_b)}e^{ikg(s_b)} - \frac{f(s_a)}{g'(s_a)}e^{ikg(s_a)}\right] + O(k^{-1}). \tag{A2}$$

In this situation the integral is governed by its end points contribution. However, if g has one stationary point lying on Γ at s^* such that $g'(s^*) = 0$ and $g''(s^*) \neq 0$, the integral is governed by the stationary point contribution, and Eq.5 can be expressed as,

$$I_\Gamma = \frac{e^{i\frac{\pi}{4}}}{2} f(s^*)\sqrt{\frac{\pi}{kg''(s^*)}}e^{ikg(s^*)} + O(k^{-1/2}). \tag{A3}$$

The first and second derivatives of the phase function g can be defined as,

$$g'(s) = \frac{dg}{ds} = \frac{d}{ds}(|\mathbf{r}(\mathbf{s})| + |\boldsymbol{\rho}(\boldsymbol{s})|) = \frac{1}{2|\mathbf{r}|}\frac{d}{ds}\mathbf{r}^2 + \frac{1}{2|\boldsymbol{\rho}|}\frac{d}{ds}\boldsymbol{\rho}^2$$
$$= \frac{\alpha + s}{|\boldsymbol{\rho}|} + \frac{\beta + s}{|\mathbf{r}|}, \tag{A4}$$

$$g''(s) = \frac{d}{ds}\left(\frac{\alpha + s}{|\boldsymbol{\rho}|} + \frac{\beta + s}{|\mathbf{r}|}\right) = \frac{|\boldsymbol{\rho}| - \frac{(\alpha+s)^2}{|\boldsymbol{\rho}|}}{\boldsymbol{\rho}^2} + \frac{|\mathbf{r}| - \frac{(\beta+s)^2}{|\mathbf{r}|}}{|\mathbf{r}|^2}$$
$$= \frac{1}{|\mathbf{r}|} + \frac{1}{|\boldsymbol{\rho}|} - \frac{(\alpha + s)^2}{|\boldsymbol{\rho}|^3} - \frac{(\beta + s)^2}{|\mathbf{r}|^3}. \tag{A5}$$

2. Evaluation of the line integral

Consider the diffraction integral of Eq.5 and the fundamental property of the Fresnel integral,

$$F[x] = U(-x) + sign(x)F[|x|], \tag{A6}$$

where U is the unit step function such as $U(-x) = 1$ if $x \leq 0$ and $U(-x) = 0$ if $x > 0$ and $sign(x) > 0$ if $x \geqslant 0$ and $sign(x) < 0$ if $x < 0$.

With a change of variable, the Fresnel integral becomes Eq.7, where t is the detour parameter, $t(s) = \epsilon_t(s)\sqrt{k|g(s^*) - g(s)|}$ with the shadow indicator $\epsilon_t(s) = 1$ if $s - s^* \geq 0$ and $\epsilon_t(s) = -1$ if $s - s^* < 0$. $G(s) = \frac{f(s)}{h(s)}$, and

$$h(s) = \begin{cases} k\frac{g'(s)}{2t(s)}, & \text{if } s \neq s^* \\ \sqrt{\frac{kg''(s^*)}{2}}, & \text{if } s = s^*. \end{cases} \tag{A7}$$

Therefore, the diffraction integral can be expressed as

$$\begin{aligned} I_\Gamma &= \int_{s_a}^{s_b} f(s)e^{ikg(s)}ds \\ &= \int_{s_a}^{\infty} f(s)e^{ikg(s)}ds - \int_{s_b}^{\infty} f(s)e^{ikg(s)}ds, \end{aligned} \tag{A8}$$

which results in the final expression of Eq.10.

3. Asymptotic expansion of the Fresnel integral

In order to find the asymptotic expansion of the Fresnel integral of Eq.8 in Eq.6 and replace it by the exact Fresnel integral of Eq.7 to eliminate the singularity of the asymptotic expansion, a new detour paramater was introduced,

$$\xi(s, P) = \epsilon_\xi(P)\sqrt{k[g(s) - |\mathbf{R}|]}, \tag{A9}$$

Where ϵ_ξ is a shadow indicator equal to 1 if P is located in the illuminated region and -1 if in the shadow.

The detour parameter ξ is then introduced in Eq.A8,

$$e^{ikg(s^*)} = e^{i\xi^2}e^{ik|\mathbf{R}|} \tag{A10}$$

$$\simeq 2\sqrt{\pi}\xi e^{-i\frac{\pi}{4}}e^{ik|\mathbf{R}|}sign(\xi)F[|\xi|]. \tag{A11}$$

Applying Eq.A11 in Eq.A8 leads to the final form of the uniform asymptotic expansion of Eq.10.

[1]C. Lu and P. Morrell, "Determination and applications of environmental costs at different sized airports - aircraft noise and engine emissions", Transportation **33**, 45-61 (2006).

[2]E.A. Meister, and R.J. Donatelle, "The impact of commercial-aircraft noise on human health: A neighborhood study in Metropolitan Minnesota", Journal of environmental health 63(4):9-15 (2000).

[3]D.L. Huff, "Noise Reduction Technologies for Turbofan Engines", NASATM-2007-214495 (2007).

[4]M. Lummer, "Maggi-Rubinowicz Diffraction Correction for Ray-Tracing Calculations of Engine Noise Shielding", 14th AIAA/CEAS Aeroacoustic Conference, AIAA paper 2008-3050 (2008).

[5]C.H. Gerhold and L.R. Clark and M.H. Dunn , "Investigation of acoustical shielding by a wedge-shaped airframe", Journal of Sound and Vibration **294**, 49-63 (2006).

[6]L.W.T. Ng and Z. Spakovszky, "Turbomachinery Noise Shielding Assessment of Advanced Aircraft Configuration", 16th AIAA/CEAS Aeroacoustics Conference, Stockholm, Sweden, AIAA Paper 2010-3914 (2010).

[7]C.A Reimann and A.F Tinetti and M.H Dunn, "Noise Prediction Studies for the Blended Wing Body Using the Fast Scattering Code", 11th AIAA/CEAS Aeroacoustics Conderence, Monterey, California, AIAA Paper 2005-2980 (2005).

[8]J.B. Keller "Geometrical Theory of Diffraction", Journal of the Optical Society of America **52 (2)**, 116-130 (1962).

[9]D.F Colas and Z.S. Spakovszky "A Turbomachinery Noise Shielding Framework Based on the Modified Theory of Physical Optics", 19th AIAA/CEAS Aeroacoustics Conference, Berlin, Germany, AIAA Paper 2013-2136 (2013).

[10]Y.Z. Umul "Modified theory of physical optics", Optics Express **12 (20)** (2004).

[11]A. Agarwal and A.P. Dowling "The calculation of acoustic shielding of engine noise by the Silent Aircraft Airframe", The Journal of the Acoustical Society of America **116 (4)** 25-39 (2004).

[12]M.H Dunn and A. Tinetti "Aeroacoustic scattering via the equivalent source method", 10th AIAA/CEAS Aeroacoustics Conference, Manchester, Great Britain, AIAA Paper 2004-2937 (2004).

[13]W.K. Lui and K.M. Li "The scattering of sound by a long cylinder above an impedance boundary", The Journal of the Acoustical Society of America **127 (2)** 664-674 (2010).

[14]Z. Maekawa "Noise Reduction by Screens", Applied Acoustics **1 (3)** 157-173 (1968).

[15]Z. Maekawa "3: Noise Reduction by Thin and Wide Barriers", John Wiley & Sons Ltd (1986).

[16]M. Rettinger (1957). Noise Level Reductions of Barriers, Journal of the SMPTE **66 (7)** 391-393.

[17]L. Lieber "Small Engine Technology (SET) - Task 13 ANOPP Noise Prediction for Small Engines", Contractor Report NASA (2000).

[18]S. Kirkup "The boundary element method in acoustics, Chap. 1" (2007)

[19]K. Miyamoto and E. Wolf "Generalization of the Maggi-Rubinowicz Theory of the Boundary Diffraction Wave - Part I", Journal of the Optical Society of America **52 (6)** 615-625 (1962).

[20]R.M. Lewist and J. Boersma "Uniform Asymptotic Theory of Edge Diffraction", Jounal of Mathematical Physics **10 (12)** (1969).

[21]R. Sommerfeld "Mathematical Theory of Diffraction", Birkhäuser Boston 2004,Pages 9-68 (2015).

[22]R. Merino-Martnez, L. Bertsch, M. Snellen and D.G. Simons "Analysis of landing gear noise during approach", 22nd AIAA/CEAS Aeroacoustics Conference, Lyon, France, AIAA Paper 2016-2769 (2016).

[23]D.G. Simons, M. Snellen, and B. Van Midden, M. Arntze and D.H.T. Bergmans "Assessment of noise level variations of aircraft flyovers using acoustic arrays", Journal of Aircraft **52 (5)** 1625-1633 (2015).

[24]R. Merino-Martnez, M. Snellen and D.G. Simons "Functional Beamforming Applied to Imaging of Flyover Noise on Landing Aircraft", Journal of Aircraft (2016).

[25]D.G. Simons, M. Snellen, R. Merino-Martinez and A. Malgoezar "Noise breakdown of landing aircraft using a microphone array and an airframe noise model", INTER-NOISE 2017 (2016).

[26]M. Snellen, R. Merino-Martnez and D.G. Simons "Assessment of the noise variability of landing aircraft using a microphone array", 5th CEAS Air and Space Conference: Challenges in European Aerospace (2015).

[27]B.M. Dunkin "Directivity and Spectral Noise Characterization of Commercial Aircraft during landing with thrust reverser engagement", Master Thesis, The Pennsylvania State University (2008).

TABLE I. Aircraft type (column 1); For each aircraft type column 2 indicates if noise shielding is expected.

Aircraft type	Shielding
Airbus 321 (A321)	No
Airbus 380 (A380)	No
Boeing 737 (B737)	No
Boeing 747 (B747)	No
Fokker 70 (F70)	Yes
McDonnell Douglas 81 (MD81)	Yes

Fig. 1. Kirchhoff integration across the circular aperture σ in the screen $\overline{\sigma}$.

Fig. 2. Volume of control,C_1, used in the Maggi Rubinowicz formulation, indicated by the dashed lines.

Fig. 3. Disk configuration for the validation of the MTPO-based method.

Fig. 4. Disk shielding for $ka = 92$: a) from[7] and b) calculated in this work using the MTPO-based method.

Fig. 5. Stripe shielding for λ=0.2 m: a) obtained with the BEM and the Ray-tracing method[4], b) calculated in this work using the MTPO-based method.

Fig. 6. Measured OSPL (normalised and averaged over the 32 microphone array) as a function of time for flyovers (landing) of a variety of aircraft types.

Fig. 7. Beamforming plots for high frequency band: (a) F70 (b) MD81[25]

Fig. 8. Limit shadow-light and source position for (a) the F70 (b) the MD81

Fig. 9. Frequency spectrum of the F70 engines. The black line indicates the measured spectrum and the gray line its approximation.

Fig. 10. OSPL calculated with averaged attenuation values, in a grid of observers on ground, a) for the F70 b) for the MD81.

Fig. 11. OSPL calculated subtracting attenuation at each frequency in a grid of observers on ground, a) for the F70 b) for the MD81.

Fig. 12. ΔOSPL in a grid of observers on ground, a) for Fig.11a) (F70), b) for Fig.11b) (MD81).

Fig. 13. Measured OSPL for Flyover 1 of the F70 and predictions with and without noise shielding

Fig. 14. Measured OSPL for Flyover 19 of the F70 and predictions with and without noise shielding.

Fig. 15. Measured OSPL for Flyover 11 of the F70 and predictions with and without noise shielding.

Fig. 16. Measured OSPL for Flyover 7 of the F70 and predictions with and without noise shielding.

Fig. 17. Measured and predicted value of noise shielding found for different flyover measurements of the F70. The dots indicate the shielding for the 20 flovers and the red dashed line - - - indicates the average value of the flyovers with noise shielding. The green dashed line - - - is the predicted value of shielding.

Fig. 18. Predictions of OSPL with and without taking noise shielding into consideration for an observer at a distance of a) 40 m and b) 160m, from the aircraft centerline (F70).